JCTC Journal of Chemical Theory and Computation

pubs.acs.org/JCTC Article

Long-Range Charge Transfer (LRCT)-Driven Enhancement of SOC and rISC in Donor-Modified MR-TADF Emitters

Hanqi Wen and Liviu Ungur*

Cite This: https://doi.org/10.1021/acs.jctc.5c01905 Read Online

ACCESS | Metrics & More | Article Recommendations | Supporting Information

ABSTRACT: Multi-Resonance Thermally Activated Delayed Fluorescence (MR-TADF) materials are leading candidates for high-efficiency narrowband Organic Light-Emitting Diodes (OLEDs), yet the electronic factors governing their reverse Intersystem Crossing (rISC) rates remain a subject of debate. In this work, we established a computational framework to investigate the factors governing the S_1-T_1 crossing in donor-modified MR-TADF emitters. By employing Orbital-Optimized DFT (OO-DFT), we achieved accurate predictions of the singlet−triplet gap (ΔE_{ST}) in close agreement with experimental data (RMSE = 0.079 eV). Using a specialized Charge Transfer descriptor $CT_{S_1T_1}$, we screened 8 candidates exhibiting Long-Range Charge Transfer (LRCT) character during the S_1-T_1 transition out of a 20-molecule database. All selected candidates show enhanced SOC upon donor modification, with Spin−Orbit Coupling Matrix Element (SOCME) values of up to 1.1 cm^{-1}. Marcus theory was applied to estimate qualitative spin-conversion trends and identify candidates with favorable crossing regimes. MECP analysis of the selected candidates shows how reorganization energy, seam accessibility, and energy-gap matching affect the S_1-T_1 crossing. ORCA ESD calculations of the elementary radiative rate k_r, ISC rate k_{ISC}, and Franck−Condon contribution k_{ISC}^{FC} were used to assess vibronic participation in the S_1-T_1 spin-flip process. These findings provide a theoretical perspective on the S_1-T_1 spin-flip mechanism and offer practical design insights for developing high-efficiency MR-TADF materials with intrinsically fast spin conversion.

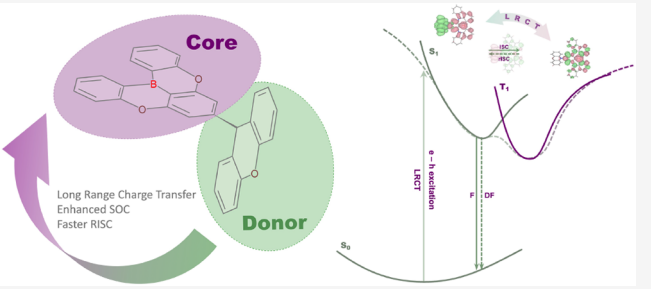

INTRODUCTION

Optical materials are important in many scenarios in our daily lives. Their light emission comes from the radiative decay of excited states, which is a process known as luminescence. Designing efficient emitters, therefore, requires maximizing the use of excitons.[1,2] Depending on the excitation method, luminescence can occur through either photoluminescence (PL) or electroluminescence (EL). EL materials are often seen in electronic devices such as sensors, display devices, etc. They always suffer from the limitation of spin statistics, where only 25% of the excitons that are in the singlet state can be used.[1,3,4] Organic light-emitting diodes (OLEDs), the most common EL devices, are central to display technologies because of their energy efficiency, flexibility, and stability. To overcome the spin statistics limit, conventional fluorescent OLEDs are often replaced by phosphorescent OLEDs, which can harvest triplet excitons but rely on expensive rare metals.[5] As a promising alternative, thermally activated delayed fluorescence (TADF) has emerged as a metal-free approach and is now widely studied as the next generation of OLED emitters.[4,6,7]

TADF emitters enable the up-conversion of dark triplet excitons to emissive singlets via reverse Intersystem Crossing (rISC).[8] This process becomes efficient when the first excited singlet−triplet energy gap ($\Delta E_{ST} = E_{S_1} - E_{T_1}$) is sufficiently small (<0.1 eV), making the spin-flip transition thermally feasible. Nevertheless, to enable the spin-prohibited rISC process, the enhancement of Spin−Orbit Coupling (SOC) and a small ΔE_{ST} are two of the most important factors.[9] Two major design paradigms, Donor−Acceptor (D−A) TADF and Multi-Resonance (MR)-TADF, aim to reduce ΔE_{ST} by minimizing the exchange interaction $\left(J = \langle \Psi_{HOMO(1)}\Psi_{LUMO(2)}|\frac{1}{r_{12}}|\Psi_{HOMO(2)}\Psi_{LUMO(1)}\rangle\right)$ between the Highest Occupied Molecular Orbital (HOMO) and the Lowest Unoccupied Molecular Orbital (LUMO) through reduced orbital spatial overlap.

Unlike traditional D−A TADF molecules with a relatively high conformational change energy during excitation due to their rigid structure, MR-TADF is designed to provide a smaller structural change while maintaining narrow-band emission.[10] In MR-TADF molecules, HOMO and LUMO

Received: November 19, 2025
Revised: July 16, 2026
Accepted: July 20, 2026

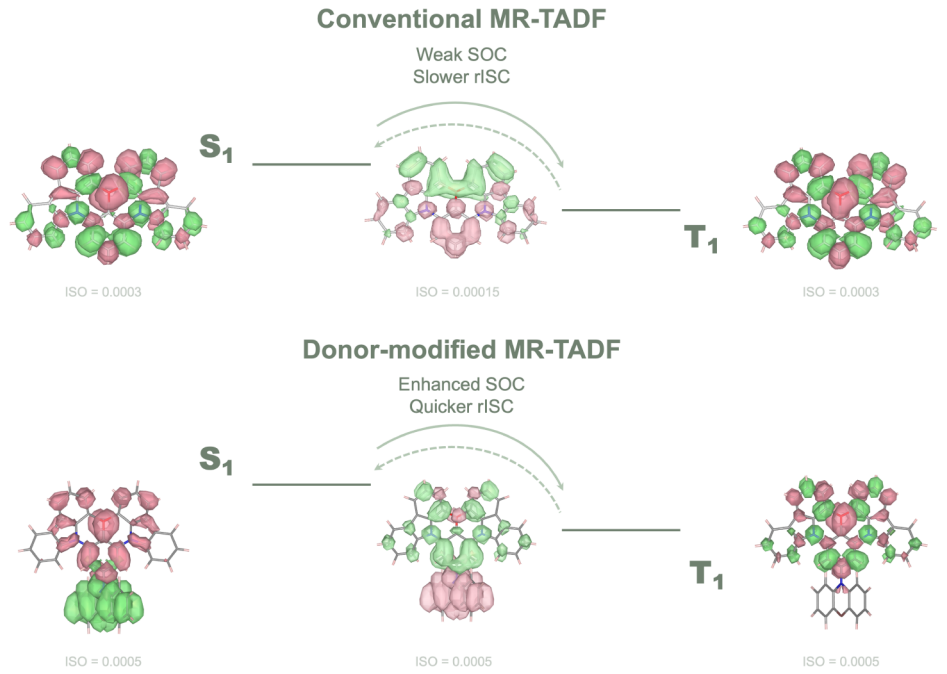

Figure 1. Schematic illustration of the rISC mechanism in conventional and donor-modified MR-TADF, showing enhanced SOC and faster rISC upon donor incorporation. From left to right, the plotted densities represent electronic density differences between S_1-S_0, T_1-S_1, and T_1-S_0, with the surface in pink representing the increase in density.

are spatially separated due to the resonance structure. This unique separation not only efficiently reduces the ΔE_{ST} but also plays a role in minimizing conformational changes in the structure. However, this leads to a similar spatial symmetry of the S_1 and T_1 electronic configurations. Therefore, SOC is typically weak due to the negligible value of the angular momentum overlap integral (El-Sayed's rule), resulting in a small SOC and a slow rISC rate (Figure 1).[11] Recent studies suggest that by introducing a peripheral donor on an MR-TADF skeleton, Long Range Charge Transfer S_1 (^{1}LRCT) and Short Range Charge Transfer T_1 (^{3}SRCT) can be constructed.[12,14] ^{1}LRCT → ^{3}SRCT process (Figure 1) brings enhanced SOC by increasing $\langle \mathrm{LRCT}^1|\hat{L}|\mathrm{SRCT}^3\rangle$, where an enhanced intersegmental charge transfer dominates the transition.

Although donor substitution is known to promote charge transfer character, the microscopic mechanism driving the rISC enhancement is not fully understood. Specifically, the nature of the efficient S_1-T_1 crossing remains ambiguous: it is unclear whether this LRCT-driven spin-flip process is best described by perturbative vibronic coupling or within the adiabatic approximation, where, instead of vibronic coupling, LRCT-induced SOC plays a more important role. To resolve this, we use Marcus theory as a qualitative model to interpret LRCT-driven crossing trends. We then compare ESD-derived k_{ISC} and k_{ISC}^{FC} for selected candidates to assess how strongly SOC-derivative vibronic terms contribute to the elementary $S_1 \rightarrow T_1$ spin-flip. In this study, we aim to utilize the charge-transfer descriptor CT (eq 3) to identify donor/core combinations that (i) efficiently enhance SOC at the intersection, (ii) maintain minimal structural displacement, and (iii) support efficient spin conversion. We then distill these results into design rules for donor-modified MR-TADF emitters.

Theoretical Background

To resolve whether this LRCT-driven spin-flip is best described by perturbative vibronic coupling or as a diabatic charge-transfer process, we must establish a rigorous computational framework. This section details the theoretical tools employed in our study: (i) OO-DFT, an advanced method for better describing charge-transfer excited states; (ii) Charge Transfer Descriptor, a quantitative metric to evaluate the extent of LRCT; (iii) Marcus Theory, used as a qualitative model to indicate charge transfer efficiency within a classical limit; (iv) ESD rate calculation, rate constant calculation based on Fermi's Golden Rule (FGR) for $S_1 \rightarrow S_0$ radiative and $S_1 \rightarrow T_1$ ISC rates; and (v) Spin-Orbit Coupling (SOC), a brief overview of the spin-orbit mean-field operator.

OO−DFT. Charge transfer excited state optimization using TD-DFT would often suffer from inaccuracy.[15] Therefore, in this work, we employed OO−DFT for excited state optimization. This approach allows the optimization of molecular orbitals explicitly for the excited state of interest by specifying the electronic configuration of the excited electron.[16,17] Unlike standard ground-state DFT, OO−DFT employs a non-Aufbau model to maintain a specific electronic configuration, ensuring that the system remains at a targeted, nonenergy-minimum state without collapsing back to the ground state. This is achieved by constraining the Self-Consistent Field (SCF) procedure to preserve the desired configuration, preventing variational collapse and enabling reliable optimization of orbitals for the excited state.[18] This method has also been benchmarked to have a good performance in calculating ΔE_{ST} for TADF emitters.[15]

https://doi.org/10.1021/acs.jctc.5c01905
J. Chem. Theory Comput. XXXX, XXX, XXX−XXX

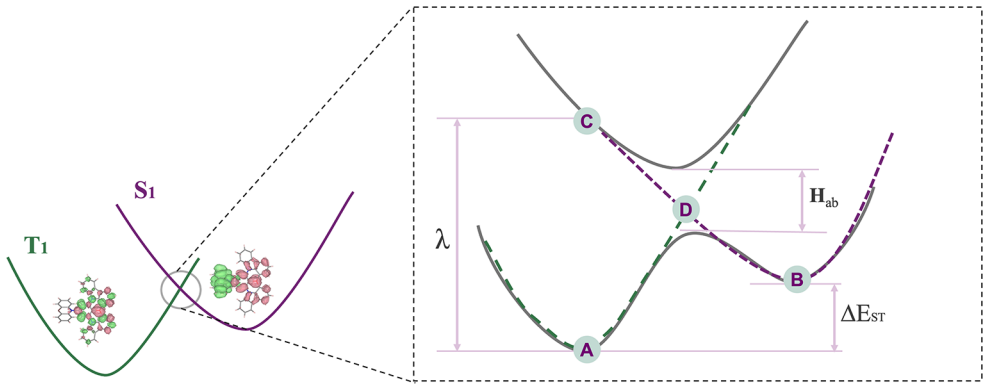

Figure 2. Schematic illustration of the Marcus charge-transfer model for LRCT in TADF emitters. Left: the potential energy surfaces of the S_1 and T_1 states with the crossing region where SOC enables the transition between diabatic states. Right: Marcus-type representation of the charge-transfer process driven by diabatic coupling. A: T_1 minimum; B: S_1 minimum; C: vertical excitation from A to the S_1 surface; D: crossing region of the S_1 and T_1 potential energy surfaces.

$$\mathbf{FC}^{\text{new}} = \mathbf{SC}^{\text{new}}\varepsilon$$
$$\mathbf{O} = (\mathbf{C}^{\text{old}})^{\dagger}\mathbf{SC}^{\text{new}}$$
$$p_j = \sum_{i=1}^{n} O_{ij} = \sum_{\nu=1}^{N}\left[\sum_{\mu=1}^{N}\left(\sum_{i=1}^{n} C_{i\mu}^{\text{old}} S_{\mu\nu}\right)\right] C_{\nu j}^{\text{new}} \tag{1}$$

The method can be summarized mathematically in eq 1. The overlap matrix element $\mathbf{O}_{ij}$ measures the overlap between the i-th old orbital and the j-th new orbital, while p_j represents the projection of the j-th new orbital onto the occupied space of the previous iteration. During each SCF step, the Fock matrix $\mathbf{F}$ is constructed using old orbitals $\mathbf{C}^{\text{old}}$, and the new orbitals $\mathbf{C}^{\text{new}}$ are obtained by solving the generalized eigenvalue problem with the overlap matrix $\mathbf{S}$.

Charge Transfer Descriptor. In order to describe charge transfer between fragments, the 1-particle Transition Density Matrix (1-TDM) is built as follows:[19,20]

$$\mathbf{D}_{\mu\nu}^{IJ} = \langle \Psi^{I}|^{\dagger} \hat{a}_{\mu}\hat{a}_{\nu}|\Psi^{J}\rangle$$
$$\langle \Psi^{I}|^{\dagger}\hat{O}_1|\Psi^{J}\rangle = \sum_{\mu\nu} \mathbf{D}_{\mu\nu}^{IJ}\langle \chi_{\mu}|\hat{O}_1|\chi_{\nu}\rangle \tag{2}$$

Here, $\hat{a}_{\mu}$ and $\hat{a}_{\nu}$ are the annihilation and creation operators for the μ-th and ν-th atomic orbitals χ_{μ} and χ_{ν}, respectively. The 1-TDM element $\mathbf{D}_{\mu\nu}^{IJ}$ quantifies the transition between states I and J mediated by the one-particle operator $\hat{O}_1$.

$$\text{CT}_{IJ} = \frac{1}{\Omega}\sum_{A,B\neq A} \Omega_{\text{AB}}^{IJ},\ \Omega = \sum_{A,B}\Omega_{AB} \tag{3}$$

Based on 1-TDM (eq 2), one can use $\Omega_{AB}^{IJ} = \sum_{\mu\in A}\sum_{\nu\in B}(\mathbf{S}^{1/2}\mathbf{D}^{IJ}\mathbf{S}^{1/2})_{\mu\nu}^2$ to describe charge transfer between fragment A and fragment B from state I to state J in the atomic orbital basis, where $S_{\mu\nu} = \int \chi_{\mu}(r)\chi_{\nu}(r)dr$. In this paper, the charge transfer descriptor is described as eq 3, where fragment A and fragment B are accordingly chosen as the core and donor, and I and J stand for the reference and excited states. For example, $\text{CT}_{S_1T_1}$ represents the charge transfer percentage between the S_1 and T_1 states.

Marcus Theory. In donor-modified TADF emitters, charge transfer character shapes the S_1/T_1 diabatic states, while $\langle \Psi_{S_1}|\hat{H}_{\text{SO}}|\Psi_{T_1}\rangle$ provides the electronic coupling between them. Within Marcus theory,[21,22] the rISC rate can be approximated as

$$k_{\text{rISC}}^{\text{M}} = \frac{2\pi}{\hbar}\frac{H_{ab}^2}{\sqrt{4\pi\lambda k_{\text{B}}T}}\exp\left[-\frac{(\Delta E_{\text{ST}} + \lambda)^2}{4\lambda k_{\text{B}}T}\right] \tag{4}$$

Here, the electronic coupling integral $H_{ab} = \langle \Psi_{S_1}|\hat{H}_{\text{SO}}|\Psi_{T_1}\rangle$ is represented by the Spin−Orbit Coupling Matrix Element (SOCME), λ is the reorganization energy, and ΔE_{ST} is the driving force for the corresponding direction in the PES. For the thermally activated rISC direction, the schematic in Figure 2 illustrates λ_{rISC} as the vertical excitation from the T_1 minimum (point A) to the S_1 surface (point C), i.e., $\lambda_{\text{rISC}} = E_C - E_A$ and $\lambda_{\text{ISC}} = E_C - E_B$.

In this work, Marcus theory is used as a classical-limit model for the $S_1 \leftrightarrow T_1$ spin-conversion rates. It can be used as a quick indicator for an efficient charge transfer process. Its limitations arise from the classical treatment of nuclear motion and the harmonic approximation of the relevant energy surfaces.[23] Therefore, to include the role of the vibronic effect in this process, the ESD calculated rate based on FGR will be discussed later.

ESD Rate Calculation. In this work, we use the ORCA ESD module[24] to calculate elementary rate constants for the $S_1 \rightarrow S_0$ radiative transition (k_{r}) and the $S_1 \rightarrow T_1$ ISC process (k_{ISC}). These rates are evaluated within a Fermi's Golden Rule framework (eq 5). For ISC, the spin−orbit coupling term $\langle \Psi_{S_1}|\hat{H}_{\text{SO}}|\Psi_{T_1}\rangle$ replaces the electric transition dipole term used for fluorescence (eq 6). To assess vibronic participation, $k_{\text{ISC}}^{\text{FC}}$ is calculated without first-derivative terms, while the full k_{ISC} includes the SOCME derivatives. Coupled-model k_{rISC} estimates require an independent experimental k_{d} input and was treated as optional consistency checks, which can be found in the Supporting Information.

$$k(\omega)_{if} = \frac{4\omega^3 n^2}{3\hbar c^3}|\langle \Psi_i|\hat{\mu}|\Psi_f\rangle|^2\,\delta(E_i - E_f \pm \hbar\omega) \tag{5}$$

The transition dipole moment is expanded as

$$\langle \Psi_i|\hat{\mu}|\Psi_f\rangle = \hat{\mu}_0 + \sum_{\nu}\left(\frac{\partial\langle \Psi_i|\hat{\mu}|\Psi_f\rangle}{\partial Q_{\nu}}\right)_{Q_{\nu}=0} Q_{\nu} \tag{6}$$

https://doi.org/10.1021/acs.jctc.5c01905
J. Chem. Theory Comput. XXXX, XXX, XXX−XXX

Table 1. Predicted and Experimental Energy Gaps between S_1 and T_1 (eV) for Proposed Molecules in the Database (RMSE = 0.079)

Series	Type	Core	Donor 1	Donor 2	Donor 3	Donor 4	Donor 5
CZ	Pred.	0.11	0.09	0.11	0.04	0.12	0.11
	Exp.	0.12[26]	–	0.18[27]	0.13[12]	–	–
DA	Pred.	0.18	0.17	0.19	0.14	0.09	0.20
	Exp.	0.18[10]	0.06[28]	–	–	–	–
DB	Pred.	0.19	0.20	0.20	0.03	0.23	0.07
	Exp.	0.15[29]	0.08[30]	–	0.06[29]	0.14[31]	–
TD	Pred.	0.19	0.20	0.20	0.04	0.28	0.13
	Exp.	–	–	0.06[32]	0.01[33]	–	0.06[34]

Spin−Orbit Coupling (SOC). In this work, SOCME values between S_1 and T_1 were evaluated using the *Spin−Orbit Mean Field* (SOMF) approximation as implemented in ORCA.[25] The SOMF approach replaces the explicit two-electron spin−orbit term ($\hat{H}^{(2)}_{SSO}$ and $\hat{H}^{(2)}_{SOO}$) from the Breit−Pauli SOC operator ($\hat{H}^{BP}_{SOC} = \hat{H}^{(1)}_{SOC} + \hat{H}^{(2)}_{SSO} + \hat{H}^{(2)}_{SOO}$) with an effective *one-electron* operator derived from the spin-averaged density, allowing efficient and accurate evaluation of SOC.

Table 2. Calculated SOCME (10^{-2} cm^{-1}) between S_1 and T_1 for Proposed Molecules in the Database[a]

Series	Core	Donor 1	Donor 2	Donor 3	Donor 4	Donor 5
CZ	3.120	2.971	2.540	17.300	3.278	2.207
DA	3.160	2.871	2.973	109.845	0.455	3.177
DB	0.002	15.400	0.263	15.600	102.001	21.083
TD	0.041	12.033	0.180	16.904	101.968	22.070

[a]M062x/def2-SVP @ S_1 Minima.

Table 3. Calculated and Experimental k_r and k_{ISC} for Reported Molecules

	$\log_{10} k_r$ (RMSE = 0.84)		$\log_{10} k_{ISC}$ (RMSE = 2.69)		
Molecule	Exp.	Calc.	Exp.	Calc.	ref.
0CZ0	8.069	8.444	4.228	6.182	26
0DA0	7.982	8.275	3.996	6.189	10
0DB0	7.690	8.151	4.204	5.529	29
1CZ2	8.107	8.425	3.881	5.053	27
1CZ3	7.023	7.614	6.301	4.903	12
1DA1	8.102	8.218	4.841	3.315	28
1DB1	8.294	8.600	4.282	4.804	30
1TD2	6.826	8.387	4.844	4.810	32
1TD3	9.120	7.237	6.384	2.594	33
1TD5	6.875	7.150	6.246	−0.221	34

RESULTS AND DISCUSSION

ΔE_{ST}, SOCME, and ESD Rate Constant

Tables 1–3 summarize key properties, including ΔE_{ST}, SOC matrix elements (SOCME = $\langle \Psi_{S_1} | \hat{H}_{SOC} | \Psi_{T_1} \rangle$) at S_1 minima, and the calculated ESD rate constants compared to the experimental data. To benchmark the accuracy of electronic structure methods, we compared ΔE_{ST} computed via OO−DFT and TD-DFT. The OO−DFT method, which directly targets the excited-state wave function while preserving orbital relaxation, yields significantly better agreement with experimental references (RMSE = 0.079 eV, Table 1) than TD-DFT (RMSE = 0.395 eV, Table S1). Molecules with reported experimental k_d are calculated to have good agreement ($\log_{10} k_{rISC}$ RMSE = 0.34) in k_{rISC} using kinetic model derived by Adachi and co-workers (Table S4). Discrepancies observed for outliers like 1CZ2 and 1DB3 in Table 5 are attributed to their large SOCME values between S_1 and T_2 (Table S2), suggesting that their spin-flip mechanism is likely dominated by the higher-lying $T_2 \rightarrow S_1$ channel rather than the S_1−T_1 pathway considered here. Notably, molecules identified with strong LRCT character consistently display enhanced $CT_{S_1T_1}$ values and larger SOCME. These trends remain robust upon validation with the explicit MECP analysis discussed below.

Selection of LRCT-Driven SOC Candidates

In Figure 3a, the candidates that exhibit the ^{1}LRCT → ^{3}SRCT transition profile are highlighted in pink. This transition was selected using charge transfer descriptors $CT_{S_0S_1}$, $CT_{S_0T_1}$, and $CT_{S_1T_1}$ calculated in Theodore.[19] For example, a molecule is identified as exhibiting ^{1}LRCT character when $CT_{S_0S_1} > 0.5$, indicating that more than 50% of the excitation at the S_1 state involves charge transfer from the donor to the core. Table 5 further summarizes the LRCT character between S_1 and T_1, using S_1 as the reference state. Candidates with $CT_{S_1T_1} > 0.7$ are highlighted in bold. The Electronic Density Difference (EDD) between T_1 and S_1 for selected candidates is plotted (Figure 3b) by subtracting S_1 electronic transition density from T_1 electronic transition density. Each candidate shows a good profile with LRCT from T_1 to S_1 states. The Marcus-type k^M_{rISC} values reported in the Supporting Information are also generally higher for the selected candidates than for the rest of the set (Figure 5 and Table S4). Although these Marcus rates are not used as the main ranking metric in this work, they qualitatively support the same screening trend by identifying candidates with a more favorable CT-mediated crossing regime.

Figure 3c illustrates the difference in CT and SOCME after donor modification compared to the core structure. All of the selected candidates (except for 1DB2) exhibit enhanced SOCME values compared to their parent core structures at both S_1 and T_1 states, indicating improved S_1-T_1 crossing efficiency upon donor substitution. Although 1TD1 and 1DB1 display weak LRCT character, they exhibit substantial SOCME values between S_1 and the higher-lying T_2 state (Figure 3c). This suggests that for these candidates, the dominant LRCT

https://doi.org/10.1021/acs.jctc.5c01905
J. Chem. Theory Comput. XXXX, XXX, XXX−XXX

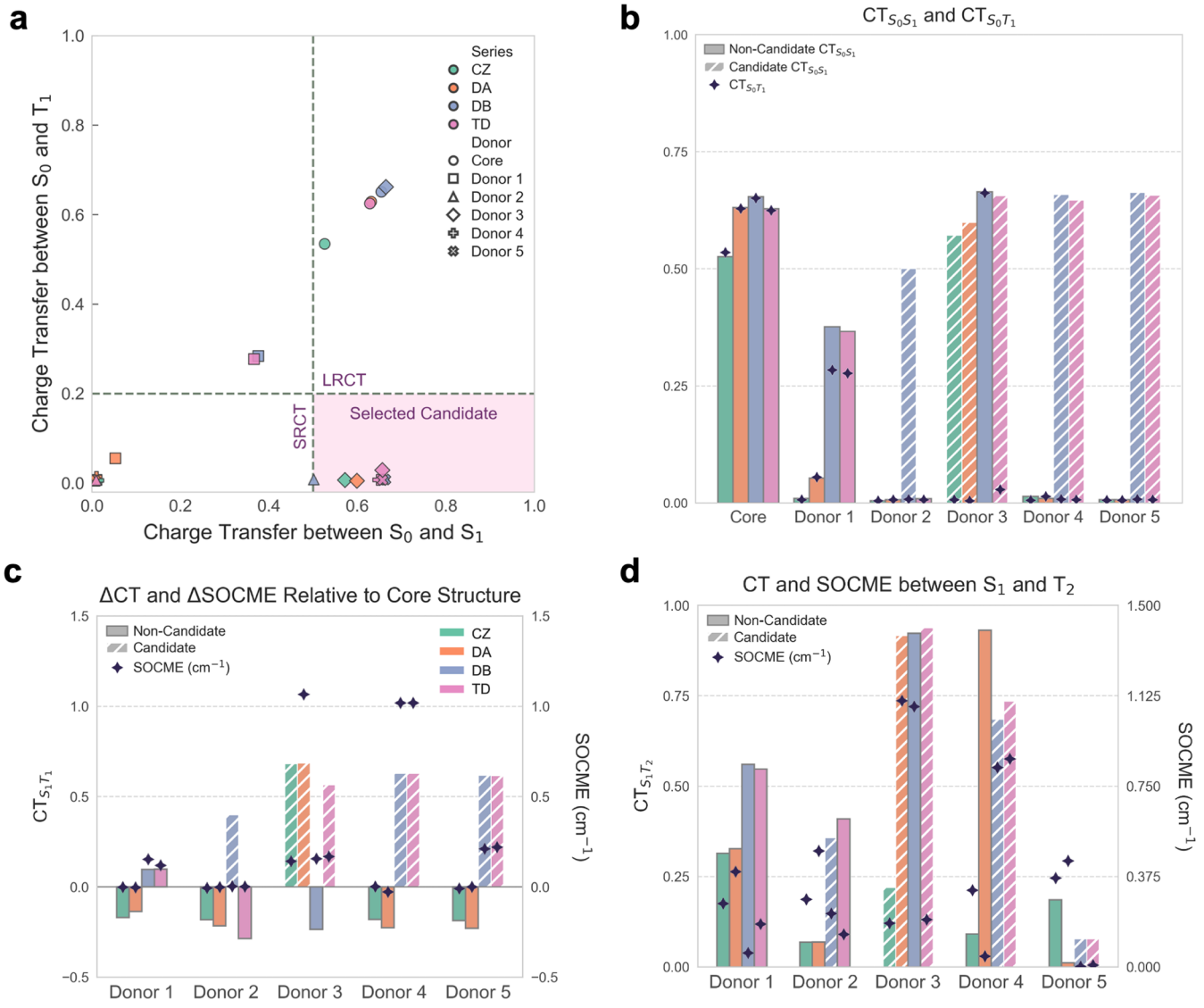

Figure 3. a): Selection criteria for LRCT-driven candidates ($CT_{S_0S_1} > 0.5$; $CT_{S_0T_1} < 0.2$). For convenience, $CT_{S_1T_1} > 0.7$ is used to describe the ^{1}LRCT → ^{3}SRCT process; **b)**: Charge transfer between S_0 and S_1 and charge transfer between S_0 and T_1, plotted by donors; **c)**: Difference in $CT_{S_1T_1}$ and SOCME after donor substitution compared to their core structure; **d)**: $CT_{S_0S_1}$ and $CT_{S_1T_2}$, plotted by donors.

process may bypass the direct $T_1 \rightarrow S_1$ route in favor of a stepwise $T_2 \rightarrow S_1$ channel. Quantitative modeling of this T_2-mediated pathway is beyond the scope of the current work because it requires a multistep kinetic treatment involving the $T_1 \rightarrow T_2$ internal conversion rate in addition to the spin-flip step.

Donors 2, 3, 4, and 5 all demonstrate potential in establishing an LRCT character during the $S_0 \rightarrow S_1$ excitation (Figure 3c). In contrast, Donor 1 (DPA) fails to induce significant LRCT character in the S_1 state. We attribute this to the conformational flexibility of the DPA moiety, which lacks the steric bulk required to enforce an orthogonal geometry. This quasi-planar conformation facilitates strong π-conjugation between the donor and the acceptor core, resulting in a state dominated by SRCT character rather than the desired LRCT. Among the studied donors, Phenoxazine (Donor 3, PXZ) exhibits exceptional performance, effectively constructing an LRCT S_1 state and an SRCT T_1 state across most core structures. A notable exception is 1DB3, where the strong LRCT character is instead identified between the S_1 and T_2 states (Figure 3d). Furthermore, while the bare core structures 0DB0 and 0TD0 are not predicted to perform highly in SOC and rate constants, functionalization with Donors 3, 4, and 5 yields a significant enhancement in both LRCT character and SOC efficiency. However, the adaptability of these donors is notably reduced in nitrogen-rich core structures (e.g., CZ and DA series). In these systems, the presence of nitrogen in the core structure shows a strong electron-donating nature, preventing the external donor from establishing the dominant LRCT character required for efficient rISC.

Analysis of Candidates

To investigate the S_1−T_1 crossing mechanism for selected candidates, we optimized the Minimum Energy Crossing Point (MECP) structures and analyzed the diabatic parameters governing the transition. High-performing candidates exhibit a robust LRCT at MECP (Figure 4). The preservation of LRCT character at the crossing point ensures that the electronic coupling (H_{ab} = SOCME) remains strong where the energy gap vanishes. Table 4 summarizes the calculated properties for

https://doi.org/10.1021/acs.jctc.5c01905
J. Chem. Theory Comput. XXXX, XXX, XXX−XXX

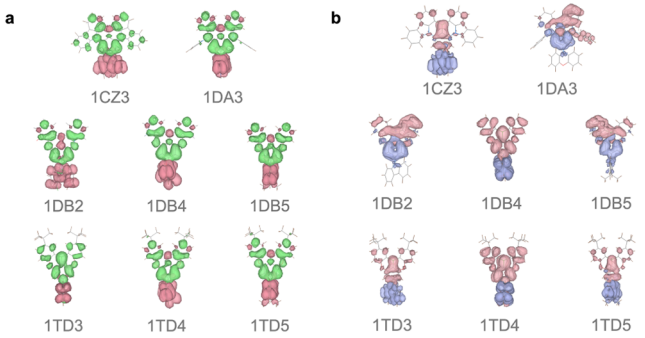

Figure 4. Electron density difference plot between T_1 and S_1 states for candidates. (isoValue = 0.0005). **a**): EDD plot at S_1 minima. Increase in density is highlighted in pink; **b**): EDD plot at the crossing point. Decrease in density is highlighted in pink.

candidate molecules. Among the candidates, 1CZ3 and 1TD3 retain strong SOCME at the crossing point (>0.16 cm^{-1}) while preserving an accessible pathway and high FC-contributed ISC to the crossing seam (Figure 5). Figure 5 shows the energy transition relative to T_1 minima and structural change at the Crossing Point (CP) from S_1 minima and T_1 minima. For spin-flip transition, this accessibility must be considered from both minima: 1CZ3 shows small displacements from both S_1 and T_1 to CP, whereas 1TD3 combines a very short $S_1 \rightarrow$ CP distortion with a still accessible $T_1 \rightarrow$ CP pathway. This indicates that the crossing region can be reached without prohibitive structural deformation in the strongest donor 3 candidates. Among the candidates, 1CZ3 and 1TD3 best combine persistent LRCT character at the crossing point, sizable CP SOCME values (>0.16 cm^{-1}), and accessible S_1/T_1-to-CP distortions (Figure 5 and Table 4). This balance is consistent with their favorable qualitative Marcus indicators, especially for 1TD3. Their ESD comparison also suggests that additional vibronic assistance is not the dominant limiting factor: Both 1TD3 and 1CZ3 present insignificant refuction from k_{ISC} to k_{ISC}^{FC}.

In comparison, 1DB2 and 1DA3 do not achieve the same balance of coupling and seam accessibility. 1DB2 has sizable SOCME at CP but requires much larger distortions from both minima, while 1DA3 combines the lowest CP SOCME with the largest S_1/T_1-to-CP displacements. Their low qualitative Marcus indicators and large separation between k_{ISC} and k_{ISC}^{FC} indicate that static LRCT/SOC coupling alone is less effective in these cases and that the calculated ISC response is more sensitive to vibronic terms.

The donor 4 pair, 1DB4 and 1TD4, shows why strong CP SOCME alone is insufficient. Although both molecules have large SOCME at the crossing point, their larger energy gap/reorganization energy mismatch gives low qualitative Marcus indicators, and their very small k_{ISC}^{FC} values relative to full k_{ISC} suggest stronger reliance on SOC-derivative vibronic contributions. The possible effect of replacing O with S from donor 3 to donor 4 should, therefore, be framed as a tentative increase in vibronic participation.

Finally, the comparison between 1DB5 and 1TD5 highlights the critical role of steric constraints in preserving the diabatic state character. Unlike 1TD5, the transition to the crossing point in 1DB5 is driven by a significant out-of-plane distortion of the core structure rather than simple donor rotation (Figure 5). This conformational change disrupts the planar π-system, shifting the transition character from the desired LRCT to a localized state on the distorted core. Consequently, this drastic structural reorganization imposes a high energetic barrier, suggesting that the transition is hindered by a severe vibronic penalty despite favorable spin−orbit coupling. In contrast, the *tert*-butyl groups in 1TD5 act as a rigid scaffold that suppresses this core distortion.

CONCLUSION

In this work, we established a computational framework to analyze the S_1-T_1 crossing mechanism in MR-TADF emitters. By integrating OO−DFT for accurate energy gap prediction (RMSE ≈ 0.08 eV) with MECP analysis, SOC evaluation, and ESD rate calculations, we identified the key factors governing the efficiency of S_1-T_1 mixing. Marcus Rate constant for rISC is also found to be a suitable qualitative indicator to filter candidates with efficient charge transfer rates under less computational cost compared to ESD rates. Looking into the selected candidates, efficient spin conversion is controlled by a balance between sizable SOC at the crossing point and an accessible structural distortion pathway connecting the minima to the crossing region. Candidates such as 1CZ3 and 1TD3 best satisfy this balance, whereas systems such as 1DB2 and 1DA3 are limited by a less favorable combination of coupling and structural accessibility. Beyond energetics, our results indicate that steric control is critical for maintaining the LRCT

Table 4. Calculated Properties of the Candidate Molecules.

Donor	Donor 2	Donor 3			Donor 4		Donor 5	
Molecule	1DB2	1CZ3	1DA3	1TD3	1DB4	1TD4	1DB5	1TD5
SOCME at CP (cm^{-1})	0.242	0.166	0.054	0.186	0.510	0.593	0.233	0.229
SOCME at S_1 (cm^{-1})	0.003	0.173	1.098	0.169	1.020	1.020	0.211	0.221
k_{rISC}^{M} (s^{-1})	1.31×10^4	3.24×10^5	6.40×10^3	1.57×10^6	5.01×10^3	1.06×10^3	7.11×10^5	5.19×10^4
k_{ISC}^{FC} (s^{-1})	8.47×10^1	3.98×10^4	3.68×10^4	3.69×10^2	4.90×10^{-1}	0.184×10^1	1.04×10^1	2.73×10^{-1}
k_{ISC} (s^{-1})	1.03×10^5	7.99×10^4	1.27×10^8	3.93×10^2	2.42×10^6	1.07×10^4	3.78×10^1	6.01×10^{-1}
k_r (s^{-1})	3.48×10^9	4.11×10^7	4.58×10^7	1.73×10^7	1.62×10^8	1.72×10^7	1.13×10^7	1.41×10^7
ΔE_{ST} (eV)	0.201	0.038	0.143	0.041	0.228	0.277	0.073	0.131
λ (eV)	0.213	0.299	0.175	0.176	0.445	0.496	0.215	0.314
RMSD (S_1/T_1; Å per atom)	0.120	0.131	0.016	0.481	0.052	0.106	0.548	0.617
RMSD (S_1/CP; Å per atom)	0.570	0.081	1.129	0.094	0.318	0.303	0.593	0.398
RMSD (T_1/CP; Å per atom)	0.612	0.211	1.119	0.523	0.328	0.384	0.310	0.377
Dihedral (°)	45.9	68.7	59.2	64.0	71.1	71.1	85.7	71.2

https://doi.org/10.1021/acs.jctc.5c01905
J. Chem. Theory Comput. XXXX, XXX, XXX−XXX

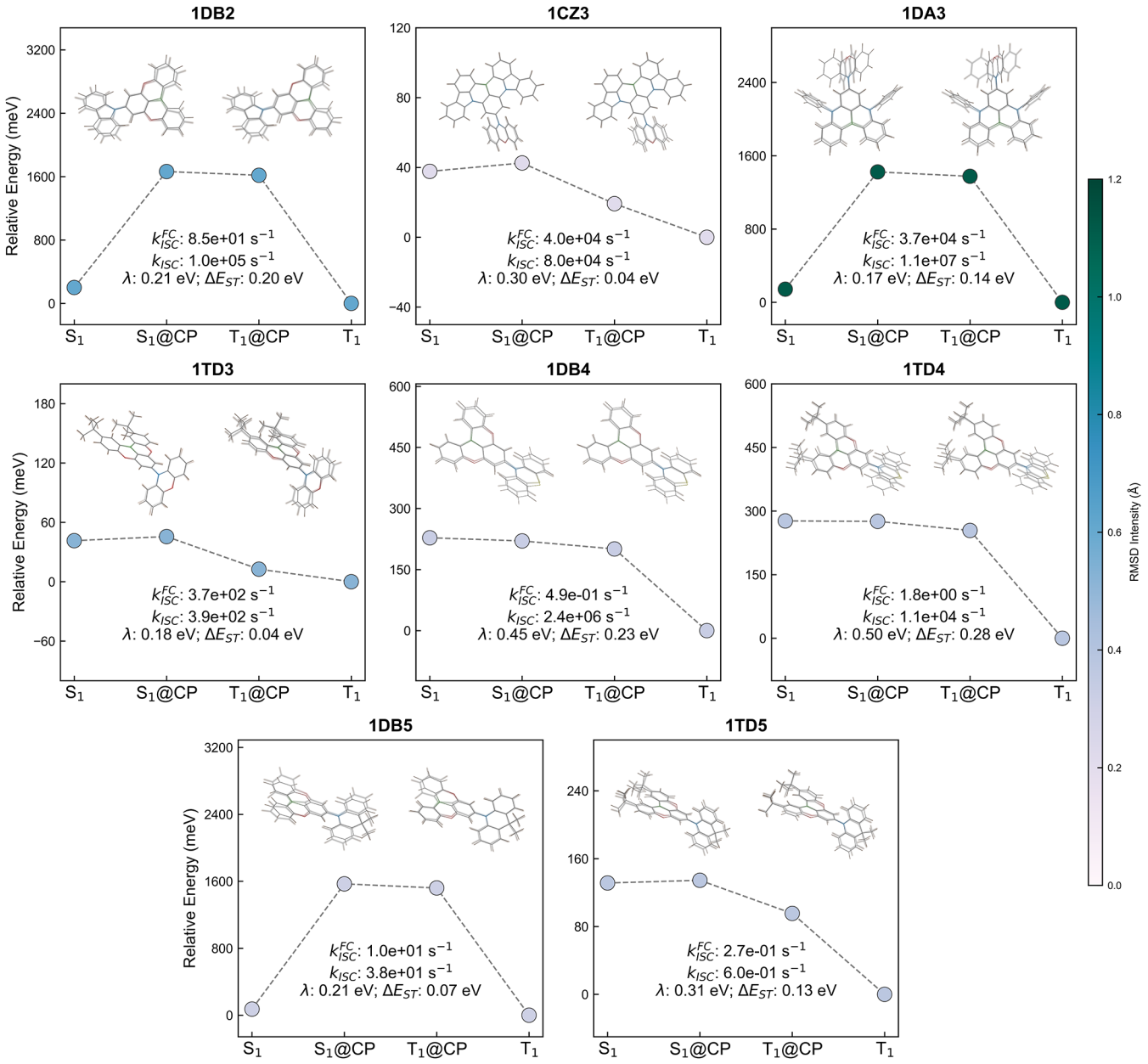

Figure 5. Energy profiles along the $S_1 \rightarrow T_1$ crossing point. Structural comparison is plotted using the crossing point structure in the background, representing the structural change from CP to S_1 minima and T_1 minima, separately.

character required for enhanced SOC at the crossing seam. Bulky substituents can help preserve donor−core decoupling, limit parasitic π-conjugation, and support efficient spin conversion.

Overall, these results provide a complementary perspective on how molecular structure influences spin conversion in MR-TADF emitters. Although the present study does not define a universal design rule, it highlights several practical features that may be useful for experimental screening, including the preservation of LRCT character, accessible S_1-T_1 crossing geometries, and steric control of donor−core coupling. We hope that these observations can help broaden the set of design metrics considered in future MR-TADF studies and provide useful scope for the exploration of new emitter structures. One limitation of the present workflow is that k_{rISC} cannot be obtained solely from the ESD-derived k_r and k_{ISC} values because the kinetic expression also requires the delayed decay rate k_d. Further integration of calculated elementary rates with reliable experimental or simulated k_d values may allow this approach to become more quantitative in future work.

METHODOLOGY

In this work, we selected five electron donors that are commonly used in organic donor−acceptor (D−A) molecules.[5,13,35] These donors were combined with four different MR-TADF core structures: CZ, DA, DB, and TD (Figure 6). All molecules in the data set, except for 1DA4, can be found in SciFinder. Some of them have also been studied in earlier publications.[10,12,26−32,34] The CZ and DA cores were chosen to study how steric effects in the core structure affect LRCT. Although both cores have similar atoms, the DA core is more distorted and nonplanar, while the CZ core is more flat and conjugated. This difference helps us understand how the core geometry influences the charge transfer when donors are

https://doi.org/10.1021/acs.jctc.5c01905
J. Chem. Theory Comput. XXXX, XXX, XXX−XXX

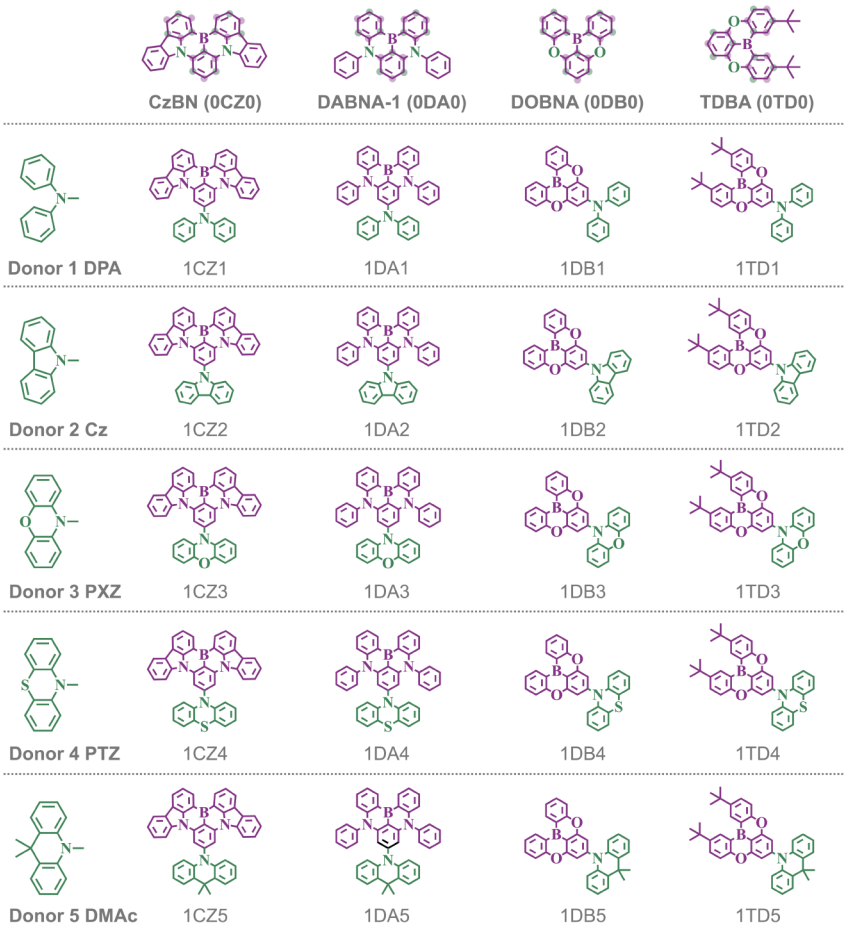

Figure 6. Table of proposed molecules in the database. All five donors are attached to four different core structures.

added. On the other hand, the DB and TD cores were chosen to examine the role of *tert*-butyl groups. These bulky side groups are known to affect the molecule's electronic structure. By comparing the TD and DB series, we can investigate how these groups contribute to charge transfer and spin−orbit coupling.

Computational Method

All quantum chemical calculations were performed in ORCA 6.[36,37] All the calculations were corrected with Grimme's D4 dispersion under a convergence threshold at `1e09` with DFT integration grids at `defGRID3`.[38−40] Structural optimization and electronic relaxation for all structures were performed at the level of theory `M062X/def-svp`.[41] Considering the strong charge transfer profile for this system, OO−DFT was applied for the structural optimization at S_1.[17,42,43] Single-point energy at point C (E_C) in (Figure 2) was calculated using OO−DFT for a vertical excitation from T_1 minima to S_1. SOCME was calculated at the S_1 minima using the M062X functional with the SOC operator RI-SOMF(1X)[25] In OO−DFT calculations, all S_1 excitation profiles were set to HOMO−LUMO. MECP calculations were conducted using sf-TDDFT in ORCA.[44,45] Upon optimization at CP, OO−DFT was again applied to obtain the single-point energy at S_1. k_{ISC} and k_r were calculated from the ESD module implemented in ORCA, and k_{rISC} for molecules with reported experimental k_d was evaluated using kinetic models with these ESD-derived k_r and k_{ISC} (see Supporting Information).[24,46−48]

Charge Transfer Calculation

The charge transfer descriptor was calculated using the post-processing software Theodore.[19] The descriptor $CT_{S_1T_1}$ refers to the charge transfer percentage between the core and donor groups, using the S_1 state as a reference. Table 5 shows the charge transfer percentage between the donor group and the core structure at T_1 using S_1 as a reference state.

Table 5. Calculated CT Percentage from T_1 to S_1

	Core	Donor 1	Donor 2	Donor 3	Donor 4	Donor 5
CZ	20.5	3.6	2.3	**88.7**	2.4	1.9
DA	24.9	11.3	3.3	**93.5**	2.2	2.0
DB	31.2	40.8	**71.2**	7.7	**94.1**	**93.0**
TD	31.2	41.0	2.6	**87.8**	**94.1**	**92.9**

■ ASSOCIATED CONTENT

Supporting Information

The Supporting Information is available free of charge at https://pubs.acs.org/doi/10.1021/acs.jctc.5c01905.

Figure S1: Electron density difference between S_1 and T_1; Table S1: Energy gap between S_1 and T_1 (eV) for proposed molecules in the database; Table S2: SOCME (cm^{-1}) between S_1 and T_2.; Table S3: Marcus rate for k_{rISC}^{M} and k_{ISC}^{M}; Table S4: Calculated rISC rates and parameters Eq. S5 (RMSE of log$k$ = 0.340); Table S5:

https://doi.org/10.1021/acs.jctc.5c01905
J. Chem. Theory Comput. XXXX, XXX, XXX−XXX

ESD-calculated elementary radiative rate k_r and ISC rate k_{ISC} (s^{-1}) for proposed molecules in the database (PDF)

AUTHOR INFORMATION

Corresponding Author

Liviu Ungur − *Department of Chemistry, National University of Singapore, Singapore 117543, Singapore;* orcid.org/0000-0001-5015-4225; Email: chmlu@nus.edu.sg

Author

Hanqi Wen − *Department of Chemistry, National University of Singapore, Singapore 117543, Singapore*

Complete contact information is available at: https://pubs.acs.org/10.1021/acs.jctc.5c01905

Notes

The authors declare no competing financial interest.

ACKNOWLEDGMENTS

L.U. and H.W. acknowledge the National University of Singapore for financing research projects A-8000709-01-00, A-1894-00-000 and A-8004827-00-00. W.H. is supported by the NUS Research Scholarship program. Ab initio calculations were performed on the ASPIRE-2A cluster (www.nscc.sg) under project 11004127. The computational resources of HPC-NUS are gratefully acknowledged.

REFERENCES

(1) Fang, M.; Yang, J.; Li, Z. Light emission of organic luminogens: Generation, mechanism and application. *Prog. Mater. Sci.* **2022**, *125*, 100914.

(2) Banerjee, S.; Singh, P.; Purkayastha, P.; Kumar Ghosh, S. Evolution of Organic Light Emitting Diode (OLED) Materials and their Impact on Display Technology. *Chem. − Asian J.* **2025**, *20* (4), No. e202401291.

(3) Baldo, M. A.; O'Brien, D. F.; Thompson, M. E.; Forrest, S. R. Excitonic singlet-triplet ratio in a semiconducting organic thin film. *Phys. Rev. B* **1999**, *60*, 14422−14428.

(4) Park, S. W.; Kim, D.; Rhee, Y. M. Overcoming the Limitation of Spin Statistics in Organic Light Emitting Diodes (OLEDs): Hot Exciton Mechanism and Its Characterization. *Int. J. Mol. Sci.* **2023**, *24*, 12362.

(5) Kim, H. J.; Yasuda, T. Narrowband Emissive Thermally Activated Delayed Fluorescence Materials. *Adv. Opt. Mater.* **2022**, *10*, 2201714.

(6) Mamada, M.; Hayakawa, M.; Ochi, J.; Hatakeyama, T. Organoboron-based multiple-resonance emitters: synthesis, structure−property correlations, and prospects. *Chem. Soc. Rev.* **2024**, *53*, 1624−1692.

(7) Yang, Z.; Mao, Z.; Xie, Z.; Zhang, Y.; Liu, S.; Zhao, J.; Xu, J.; Chi, Z.; Aldred, M. P. Recent advances in organic thermally activated delayed fluorescence materials. *Chem. Soc. Rev.* **2017**, *46*, 915−1016.

(8) Uoyama, H.; Goushi, K.; Shizu, K.; Nomura, H.; Adachi, C. Highly efficient organic light-emitting diodes from delayed fluorescence. *Nature* **2012**, *492*, 234−238.

(9) Di Maiolo, F.; Phan Huu, D. K. A.; Giavazzi, D.; Landi, A.; Racchi, O.; Painelli, A. Shedding light on thermally-activated delayed fluorescence. *Chem. Sci.* **2024**, *15*, 5434−5450.

(10) Hatakeyama, T.; Shiren, K.; Nakajima, K.; Nomura, S.; Nakatsuka, S.; Kinoshita, K.; Ni, J.; Ono, Y.; Ikuta, T. Ultrapure Blue Thermally Activated Delayed Fluorescence Molecules: Efficient HOMO−LUMO Separation by the Multiple Resonance Effect. *Adv. Mater.* **2016**, *28*, 2777−2781.

(11) Lower, S. K.; El-Sayed, M. A. The Triplet State and Molecular Electronic Processes in Organic Molecules. *Chem. Rev.* **1966**, *66*, 199−241.

(12) Huang, Z.; Xie, H.; Miao, J.; Wei, Y.; Zou, Y.; Hua, T.; Cao, X.; Yang, C. Charge Transfer Excited State Promoted Multiple Resonance Delayed Fluorescence Emitter for High-Performance Narrowband Electroluminescence. *J. Am. Chem. Soc.* **2023**, *145*, 12550−12560.

(13) Du, M.; Zhou, J.; Luo, X.; Duan, L.; Zhang, D. A perspective on boron-based multiple resonance narrowband emitters and devices. *Moore More* **2024**, *1*, 5.

(14) Hou, C.-L.; Guo, S.; Sun, Y.-F.; Hu, J.-X.; Liao, H.-J.; Li, X.; Lin, F.-L.; Meng, L.; Chen, X.-L.; Lu, C.-Z. Tuning photoluminescence and electroluminescence of multi-resonance thermally activated delayed fluorescence emitters through peripheral donor modification for highly efficient deep-blue OLEDs. *Chem. Eng. J.* **2025**, *508*, 160880.

(15) Kunze, L.; Hansen, A.; Grimme, S.; Mewes, J.-M. PCM-ROKS for the Description of Charge-Transfer States in Solution: Singlet−Triplet Gaps with Chemical Accuracy from Open-Shell Kohn−Sham Reaction-Field Calculations. *J. Phys. Chem. Lett.* **2021**, *12*, 8470−8480.

(16) Hait, D.; Head-Gordon, M. Orbital Optimized Density Functional Theory for Electronic Excited States. *J. Phys. Chem. Lett.* **2021**, *12*, 4517−4529.

(17) Selenius, E.; Sigurdarson, A. E.; Schmerwitz, Y. L. A.; Levi, G. Orbital-Optimized Versus Time-Dependent Density Functional Calculations of Intramolecular Charge Transfer Excited States. *J. Chem. Theory Comput.* **2024**, *20*, 3809−3822.

(18) Ye, H.-Z.; Welborn, M.; Ricke, N. D.; Van Voorhis, T. Delta-SCF: A direct energy-targeting method to mean-field excited states. *J. Chem. Phys.* **2017**, *147*, 214104.

(19) Plasser, F. TheoDORE: A toolbox for a detailed and automated analysis of electronic excited state computations. *J. Chem. Phys.* **2020**, *152*, 084108.

(20) Plasser, F.; Lischka, H. Analysis of Excitonic and Charge Transfer Interactions from Quantum Chemical Calculations. *J. Chem. Theory Comput.* **2012**, *8*, 2777−2789.

(21) Marcus, R.; Sutin, N. Electron transfers in chemistry and biology. *Biochim. Biophys. Acta* **1985**, *811*, 265−322.

(22) Yu, J.; Tang, J.; Ma, Z.; Wang, H. Enhancing Reverse Intersystem Crossing in TSCT-TADF Emitters: Heavy Atom Modulation of Multiresonance Acceptors. *J. Phys. Chem. A* **2025**, *129*, 459−469.

(23) Richardson, J. O.; Bauer, R.; Thoss, M. Semiclassical Green's functions and an instanton formulation of electron-transfer rates in the nonadiabatic limit. *J. Chem. Phys.* **2015**, *143*, 134115.

(24) De Souza, B.; Neese, F.; Izsák, R. On the theoretical prediction of fluorescence rates from first principles using the path integral approach. *J. Chem. Phys.* **2018**, *148*, 034104.

(25) Neese, F. Efficient and accurate approximations to the molecular spin-orbit coupling operator and their use in molecular g-tensor calculations. *J. Chem. Phys.* **2005**, *122*, 034107.

(26) Xu, S.; Yang, Q.; Zhang, Y.; Li, H.; Xue, Q.; Xie, G.; Gu, M.; Jin, J.; Huang, L.; Chen, R. Solution-processed multi-resonance organic light-emitting diodes with high efficiency and narrowband emission. *Chin. Chem. Lett.* **2021**, *32*, 1372−1376.

(27) Lee, Y.; Chan, C.; Tanaka, M.; Mamada, M.; Balijapalli, U.; Tsuchiya, Y.; Nakanotani, H.; Hatakeyama, T.; Adachi, C. Investigating HOMO Energy Levels of Terminal Emitters for Realizing High-Brightness and Stable TADF-Assisted Fluorescence Organic Light-Emitting Diodes. *Adv. Electron. Mater.* **2021**, *7*, 2001090.

(28) Wang, Y.; Duan, Y.; Guo, R.; Ye, S.; Di, K.; Zhang, W.; Zhuang, S.; Wang, L. A periphery cladding strategy to improve the performance of narrowband emitters, achieving deep-blue OLEDs with CIEy < 0.08 and external quantum efficiency approaching 20%. *Org. Electron.* **2021**, *97*, 106275.

(29) Hirai, H.; Nakajima, K.; Nakatsuka, S.; Shiren, K.; Ni, J.; Nomura, S.; Ikuta, T.; Hatakeyama, T. One-Step Borylation of 1,3-Diaryloxybenzenes Towards Efficient Materials for Organic Light-Emitting Diodes. *Angew. Chem., Int. Ed.* **2015**, *54*, 13581−13585.
(30) Jung, S.; Cheung, W.-L.; Li, S.-J.; Wang, M.; Li, W.; Wang, C.; Song, X.; Wei, G.; Song, Q.; Chen, S. S.; Cai, W.; Ng, M.; Tang, W. K.; Tang, M.-C. Enhancing operational stability of OLEDs based on subatomic modified thermally activated delayed fluorescence compounds. *Nat. Commun.* **2023**, *14*, 6481.
(31) Zhang, F.; Li, G.; Shi, C.; Li, F.; Li, Q.; Yuan, A. Tunable multimode emission induced by charge transfer and multiple resonance effect. *Dyes Pigm.* **2024**, *222*, 111902.
(32) Jin, P.; Yang, X.; Su, W.-T.; Zhan, S.-H.; Chen, X.; Sun, H.; Yang, B.; Su, S.-J.; Hu, J.-Y. Narrow emission band ultraviolet/deep-blue thermally activated delayed fluorescence emitters modified with carbazole/carboline as a donor. *J. Mater. Chem. C* **2024**, *12*, 19498−19505.
(33) Xie, H.; Huang, Z.; Li, N.; Hua, T.; Miao, J.; Yang, C. Rational molecular design of TADF emitters towards highly efficient yellow electroluminescence with a nearly 30% external quantum efficiency and low roll-off. *J. Mater. Chem. C* **2022**, *10*, 11239−11245.
(34) Gao, Y.; Wang, Y.; Guo, Z.; Wan, Y.; Xue, Z.; Han, Y.; Yang, W.; Ma, X. Ultrafast photophysics of an orange−red thermally activated delayed fluorescence emitter: the role of external structural restraint. *Chem. Sci.* **2024**, *15*, 6410−6420.
(35) Zhang, D.; Cai, M.; Zhang, Y.; Zhang, D.; Duan, L. Sterically shielded blue thermally activated delayed fluorescence emitters with improved efficiency and stability. *Mater. Horiz.* **2016**, *3*, 145−151.
(36) Neese, F.; Wennmohs, F.; Becker, U.; Riplinger, C. The ORCA quantum chemistry program package. *J. Chem. Phys.* **2020**, *152*, 224108.
(37) Neese, F. Software Update: The ORCA Program System—Version 6.0. *WIREs Comput. Mol. Sci.* **2025**, *15* (2), No. e70019.
(38) Neese, F. The SHARK integral generation and digestion system. *J. Comput. Chem.* **2023**, *44* (3), 381.
(39) Wittmann, L.; Gordiy, I.; Friede, M.; Helmich-Paris, B.; Grimme, S.; Hansen, A.; Bursch, M. Extension of the D3 and D4 london dispersion corrections to the full actinides series. *Phys. Chem. Chem. Phys.* **2024**, *26*, 21379−21394.
(40) Helmich-Paris, B.; de Souza, B.; Neese, F.; Izsák, R. An improved chain of spheres for exchange algorithm. *J. Chem. Phys.* **2021**, *155*, 104109.
(41) Zhao, Y.; Truhlar, D. G. The M06 suite of density functionals for main group thermochemistry, thermochemical kinetics, noncovalent interactions, excited states, and transition elements: two new functionals and systematic testing of four M06-class functionals and 12 other functionals. *Theor. Chem. Acc.* **2008**, *120*, 215−241.
(42) Schmerwitz, Y.; Selenius, E.; Levi, G. Freeze-and-release direct optimization method for variational calculations of excited electronic states. *J. Chem. Theory Comput.* **2026**, *7*, 3571−3584.
(43) Schmerwitz, Y.; Ivanov, A.; Jonsson, E.; Jonsson, H.; Levi, G. Variational density functional calculations of excited states: Conical intersection and avoided crossing in ethylene bond twisting. *J. Phys. Chem. Lett.* **2022**, *13*, 3990−3999.
(44) Casanova, D.; Krylov, A. I. Spin-flip methods in quantum chemistry. *Phys. Chem. Chem. Phys.* **2020**, *22*, 4326−4342.
(45) Maeda, S.; Ohno, K.; Morokuma, K. Updated Branching Plane for Finding Conical Intersections without Coupling Derivative Vectors. *J. Chem. Theory Comput.* **2010**, *6*, 1538−1545.
(46) Zhang, Q.; Kuwabara, H.; Potscavage, W. J.; Huang, S.; Hatae, Y.; Shibata, T.; Adachi, C. Anthraquinone-Based Intramolecular Charge-Transfer Compounds: Computational Molecular Design, Thermally Activated Delayed Fluorescence, and Highly Efficient Red Electroluminescence. *J. Am. Chem. Soc.* **2014**, *136*, 18070−18081.
(47) Kaji, H.; Suzuki, H.; Fukushima, T.; Shizu, K.; Suzuki, K.; Kubo, S.; Komino, T.; Oiwa, H.; Suzuki, F.; Wakamiya, A.; Murata, Y.; Adachi, C. Purely organic electroluminescent material realizing 100% conversion from electricity to light. *Nat. Commun.* **2015**, *6*, 8476.
(48) Goushi, K.; Yoshida, K.; Sato, K.; Adachi, C. Organic light-emitting diodes employing efficient reverse intersystem crossing for triplet-to-singlet state conversion. *Nat. Photonics* **2012**, *6*, 253−258.

https://doi.org/10.1021/acs.jctc.5c01905
J. Chem. Theory Comput. XXXX, XXX, XXX−XXX